Synchrotron radiation study of the electronic structure of multiwalled carbon nanotubes

Synchrotron radiation study of the electronic structure of multiwalled carbon nanotubes

J Schiessling[1], **L Kjeldgaard**[1,4], **F Rohmund**[2], **L K L Falk**[2],
E E B Campbell[2], **J Nordgren**[1] **and P A Brühwiler**[1,3]

[1] Department of Physics, Uppsala University, Box 530, SE-751 21 Uppsala, Sweden
[2] Chalmers University of Technology, SE-412 96 Gothenburg, Sweden
[3] EMPA, Lerchenfeldstrasse 5, CH-9014 St Gallen, Switzerland

E-mail: Joachim.Schiessling@fysik.uu.se and Paul.Bruehwiler@empa.ch

Abstract
We present photoelectron (PE) and x-ray absorption spectra (XAS) of
macroscopically aligned multiwalled carbon nanotubes. We identify the peaks
in the valence PE spectra with regions of high density of states through
comparison to calculations for graphite. Finally, we outline and illustrate a
simple method for using XAS to determine the average alignment of a nanotube
sample.

1. Introduction

Carbon nanotubes (CNT) are currently of high interest. Their intrinsic properties, such as
a nanometric cross section, high aspect ratio, and good thermal and electric conductivity,
suggest a high applications potential. The electronic properties of CNT vary from metallic to
semiconducting depending on their helicity and diameter as well as, in principle, on their mutual
arrangement [1, 2]. For many properties, CNT can be modelled as tubular graphite [3, 4], as
has been demonstrated in theoretical and experimental studies [5–7].

In recent years much progress has been made with the production of aligned nanotube
samples [8–13], and one could expect further progress in the understanding of CNT electronic
structure. Earlier electronic structure studies employing x-ray absorption spectroscopy (XAS)
and photoelectron spectroscopy (PES) have provided a picture of CNT as being largely
similar to graphite [7, 14], whereas more recent spectroscopy work has stressed differences.
Momentum-resolved valence PES, e.g., was reported to detect only a small electronic band
dispersion for vertically aligned multiwalled carbon nanotubes (MWNT) [15]. The C 1s line
is typically very broad and asymmetric in data presented so far. This has been attributed to
the metallicity of the nanotubes in the sample [16, 17], to an exotically enhanced lifetime

---

[4] Present address: MAX-lab, University of Lund, Box 118, SE-221 00 Lund, Sweden.

broadening [14], and to oxidation [18]. XAS and PES data are found to vary with sample position [17, 19]. One PES study found little dependence of the spectra on the emission angle, which was attributed to states in the bulk and at the surface being virtually identical [20], which one can approximately claim for graphite [21]. Thus, there appears to be some consensus that the electronic structure of CNT should and does approach that of graphite, but there are notable exceptions to this expectation.

We present PES and XAS data for macroscopically aligned MWNT. Scanning electron microscopy (SEM) was used to visually characterize the samples before the analysis using the electron spectroscopies. Core level PES was used to study the local atomic structure of the sample, and valence PES to characterize the extended states. C 1s XAS was applied to study the unoccupied states and, for the first time, the spatial orientation of the MWNT in a macroscopic sample. We find a strong position dependence of the spectra, with good consistency between the different methods. This variation is ascribed to variations in the density of structural defects in the nanotubes. We rule out a significant contribution from other carbon species to the spectra using XAS. For a sample relatively free of defects, we confirm the expected strong similarity with graphite, showing for the first time excellent agreement for the valence spectrum. All valence spectra show close agreement with the graphite DOS in the placement of critical points. We also measure the narrowest C 1s line of any MWNT sample to date. Combined with our other observations, this suggests that defects were important for measurements thus far, and that previous claims of novel physics were premature.

2. Experimental details

PES and XAS spectra were taken at Beamline D1011 [22, 23] at MAX-lab in Lund, Sweden, which is comprised of a modified SX700 monochromator and a high efficiency electron spectrometer of modified Scienta type with a 20 cm mean radius. The angle between the incident light and photoelectron analyser is 40°. For the XAS measurements the secondary electrons were collected using a multi-channel-plate electron yield detector. The base pressure in the sample preparation chamber was 6×10^{-10} and 1×10^{-10} mbar in the analysis chamber.

The MWNT were grown *ex situ* on a silicon wafer using thermal vapour deposition [9]. TEM (not shown) revealed tubes consisting of on average 20 layers, with an outer diameter of the order of 40 nm, and an interlayer spacing of 3.5 ± 0.1 Å. This is similar to the theoretical value of 3.39 Å [24] and experimental determinations for other samples of 3.4 Å [25, 26]. The sample was annealed in the preparation chamber to 320 °C for 30 min to remove possible contamination. SEM was used to survey the sample, and nothing deviating from the images shown in figure 1 below was observed, suggesting that there were negligible quantities of obvious impurities such as amorphous carbon or graphite flakes.

The XAS spectra presented here are corrected for the structured throughput of first- and second-order synchrotron light [27]. In normal incidence, the illuminated sample area was 1 mm (vertical) × 0.9 mm (horizontal). In normal emission PES, the photoelectron analyser images an area of a few tenths of a millimetre (vertical) by a few millimetres (horizontal), and the spectra are thus representative of a macroscopic area of this surface. PES and XAS measurements were taken all over the sample, and a variety of lineshapes were found. In the following sections we present measurements from four sample spots (A)–(D) which are representative of the lineshapes observed. The total experimental resolution was 150 meV (200 meV) for the valence (C 1s) PES spectra, and 100 meV for the C 1s XAS spectra. The incidence angles of the synchrotron light are the same in PES and XAS for a given sample position.

The PES valence data were aligned at the Fermi level, whereas the core level data are not aligned, so the core level binding energy scale is not to be used for comparison due to
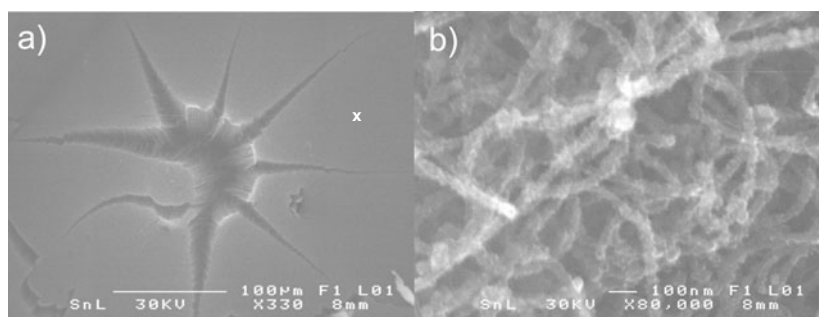
Figure 1. Scanning electron microscope images of samples similar to that studied here. (a) A view of the surface, including an open crack which displays good macroscopic alignment perpendicular to the surface. The crack shown is viewed from the top. The centre of the crack is the dark area, from which the MWNT stripes in the image emerge largely in the radial direction towards the surface of the sample. (b) A more highly magnified image of the 'flat' region marked by a cross in (a), revealing a more random distribution of tube orientations on the 100 nm scale at the surface.

possible charging effects. Photon energy calibration of the absorption spectra was carried out by measuring the C 1s line excited by first- and second-order light. O 1s XPS spectra showed slight oxygen contamination on the sample[5]; we presume that this contamination is responsible for a portion of what we describe below as defects. However, one should also note that highly oriented pyrolytic graphite (HOPG) can also show large oxygen content, without strongly affecting C 1s and valence band spectra. Thus the level to which the oxygen signal corresponds to defects is not quantifiable. No Fe 3p signal due to the catalyst was found in the spectra, giving an upper limit on the ratio Fe to C in the sample of 0.05%.

3. Results

3.1. Microscopy

Figure 1 shows a SEM image of the sample. The film surface is flat on the 100 μm scale. At some spots the film surface showed cracks, such as the one displayed in figure 1(a). Because of the small number of cracks most of the spectra are representative of the 'flat' surface regions, but it was not possible to monitor this for the present measurements. In an optical microscope inspection of the sample before the measurement, no graphite flake structure was observed. Some impurities in the (sub-) 100 nm range, very dispersed, are seen in SEM; see figure 1(b) for an illustration. At the sidewalls of the crack a high degree of alignment perpendicular to the macroscopic surface can be seen. The length of the tubes, estimated from SEM, is more than 60 μm. Figure 1(b) shows a magnification of the flat surface region and reveals a disordered structure on the 100 nm scale within the available probe depth. These images are typical for what was observed at different positions and for different samples.

3.2. Core level spectroscopy

We begin with a discussion of the C 1s photoemission spectra. Due to the large local component in the relative binding energy for core level spectra, PES often provides structural information [28]. We find a variation of lineshape over the sample, suggesting sample inhomogeneities, which we discuss below. Data taken at four sample positions labelled (A)–(D)

---

[5] The oxygen contamination of spot (A) was, relative to that at spots (B), (C), and (D), 29 ± 16, 44 ± 24, and $44\pm29\%$, respectively, with absolute upper O/C ratios of $12 \pm 6\%$.
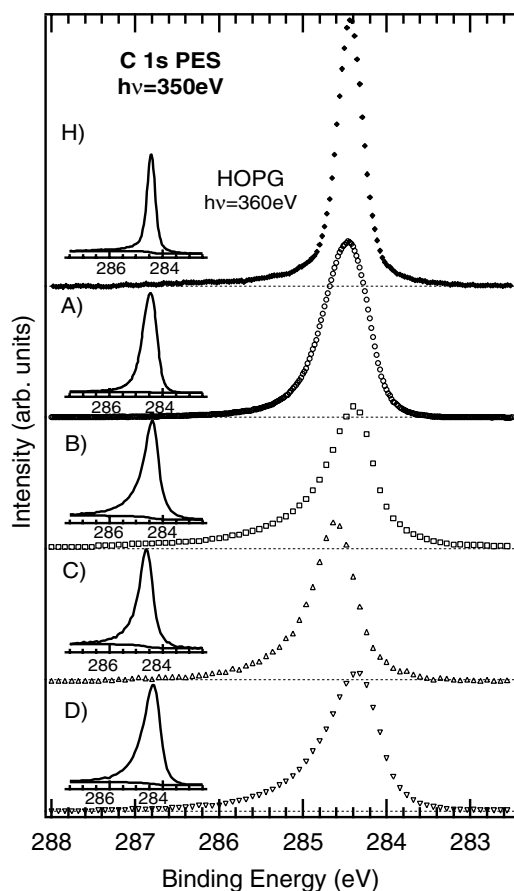
Figure 2. (A)–(D) C 1s photoemission of MWNT taken at the sample positions indicated, after subtraction of a Shirley background. In the insets an illustration of the background fitting procedure including the raw data is shown. The photoelectron emission angle was $40°$ (spectrum (B): $30°$) from the sample normal. The difference in measured area between the cases for the two emission angles is $\cos 30° / \cos 40° = 1.13$. (H) Photoemission from [29] in normal emission.

are shown in figure 2. For comparison a C 1s spectrum from HOPG [29] is also included. The raw data show that the contribution of inelastically scattered photoelectrons varies with sample position. Spot (A) has only a minor contribution, whereas the contribution is significant in spots (B)–(C). The same trend is observed for the valence spectra, as shown below. After background subtraction all spectra are normalized to equal areas in the energy region presented.

As shown in table 1, the FWHM of the spectra from all spots is substantially larger than that of HOPG. The most symmetric lineshape is found at spot (A), whereas spectra (B)–(D) all have a significant tail on the high energy side. Notably, the FWHM increases roughly in proportion to the background due to inelastically scattered electrons. Spectrum (A) has the lineshape approximating that of HOPG most closely out of the present series of spectra. This variation with sample position is consistent with effects of disorder. To quantify the asymmetry we calculate the standard deviation. This confirms the visual perception that spectrum (A) is closest to that of graphite.

A core level lineshape can be roughly explained as being due to the following contributions [28]: core hole lifetime, excitation of vibrations and electron–hole pairs, and

Table 1. Lineshape parameters of the C 1s core level spectra shown in figure 2, after the illustrated Shirley background subtraction and normalization. See the text for more details.

	FWHM (eV)	Standard deviation (eV)
HOPG [29]	0.36	0.38
A	0.63	0.44
B	0.66	0.66
C	0.62	0.56
D	0.77	0.57

Table 2. Widths of the C 1s core level lineshape from the available literature.

	FWHM (eV)	Resolution (eV)
HOPG [29]	0.36	0.30
SWNT bundles [16]	0.58	0.20
Present work, position A	0.63	0.20
Fullerenes, 'bucky paper' [17]	0.67	0.35
SWNT bundles [17]	0.67	0.35
Aligned MWNT [20]	0.68	0.20
Random MWNT [20]	0.68	0.20
MWNT [14]	1.10	0.80[a]
Aligned MWNT [19]	1.11	Not reported
Powder MWNT [52]	1.55	Not reported

[a] Estimated from the reported width of 1 eV for graphite.

surface core level shifts (SCLS). Additionally, structural information is given via chemical shifts due to atomic neighbour distributions, including variations due to, e.g., disorder and defects. A distribution of different tube diameters and contaminants must also be considered. The first three of these sources largely explain the case of graphite, with a Lorentzian broadening due to the core hole lifetime of $\Gamma_L \leqslant 160$ meV [30, 31], vibrational broadening of $\Gamma_{vib} \leqslant 100$ meV [30, 31], and SCLS of approximately 120 meV [31].

In previous investigations, the greater broadening of the C 1s line for MWNT [14] and for SWNT [17] samples compared to graphite was attributed to a dramatically lowered core hole lifetime. Comparing the FHWM of graphite (1.0 eV) and MWNT (1.1 eV) reported in [14], this implies a lifetime broadening of the order of 270 meV. A broadening of 220 meV is reported in [17]. If one compares the Lorentzian width due to the core hole lifetime broadening of graphite ($\leqslant 160$ meV) [30, 31] or C_{60} (≈ 150 meV) [32] and smaller molecules (≈ 97 meV) [33], such a large increase is not physically motivated [21, 34]. Table 2 summarizes core level studies found in the literature. Spot (A) in the present work yielded one of the sharpest lineshapes reported for MWNT. Clearly all MWNT studies obtain a significantly larger FWHM than found for graphite, ranging from 0.63 to 1.55 eV. The variation in width and shapes observed in figure 2 and summarized in table 2 suggests that the variability between samples and within samples is not yet minimized. This variation suggests that effects such as structural defects and contaminants [28] cause the relatively large broadening of the C 1s line observed in all CNT spectra so far, including the present best case.

Electron–hole pairs and other quasiparticle excitations surely contribute at some level to the observed line asymmetries, but the well-studied case of graphite suggests that this contribution should be minor [29–31]. We observe asymmetries in our own data which vary with sample position, indicating the important role of defects and inhomogeneities for this spectral parameter in state-of-the-art samples as well. As regards the asymmetry, the C 1s

spectra of graphite are particularly sensitive to any charge transfer effects [29], which could be brought about by defects and/or contaminants. Local shifts can also be due to tubes lying partially on the surface giving rise to final state field effects as for the SCLS [31]. For cases of semiconducting tubes or weak interconnects, small charging effects should also be considered, which may not be simple to discern from the Fermi energy region spectra due to the slowly varying shape of the valence density of states (DOS) [29]. Thus, the remaining difference between graphite and CNT awaits the production of significantly better-ordered samples in terms of atomic structure, but also in terms of macroscopic arrangement. What is clear is that sample inhomogeneities must play a dominant role in the observed C 1s width and asymmetries.

Due to the strong influence of inhomogeneities on the core level lineshape it is not possible to identify and quantify components of pure MWNT and defect induced/modified structures of the C 1s lineshape. Nevertheless a qualitative criterion for the amount of defect structure and other disorder is given by the linewidth and standard deviation, as summarized for the present sample in table 1, with smaller values indicating higher integrity in the MWNT architecture.

3.3. Valence spectroscopy

We focus now on the valence PES to investigate the electronic properties. The kinetic energy of the photoelectrons and, with it, the mean free path are comparable to those from the core level study in section 3.2, and thus the same samples are probed in both measurements. Figure 3(a) displays the valence band spectra of the corresponding positions together with photoemission from HOPG [29].

The background intensity due to inelastically scattered electrons, which in this case can be appreciated, e.g., at 23 eV binding energy, varies from position to position on the sample quite similarly to that in the C 1s spectra. The intensity at 5.5 eV follows the same trend, as does the width of the step-like shape at 2.8 eV. From the fact that these spots show a higher background due to inelastically scattered electrons in valence PES and C 1s, it is natural to assume that they are characterized by a higher density of defects, and we therefore assign the intensity at 5.5 eV to defect structures. Looking at the details of the lineshape, spectrum (A) shows the lowest background from inelastically scattered electrons and the sharpest structures. In addition, spot (A) and HOPG are similar in the range from E_F to 10 eV, with excellent agreement near E_F. In the present study there is no Fermi edge-like intensity, i.e., the tubes are not measurably metallic.

The overall similarity of the spectra with those of HOPG suggests that one can explain at least some of the observations for the MWNT in terms of the graphite band structure. Figure 3(b) shows this to indeed be the case, displaying a strong correlation between the critical points of the band structure of graphite and the features of the MWNT spectra, with a small expansion of the theoretical energy scale to account for self-energy effects [35]. The good agreement is not surprising in the ideal case, since a MWNT with large diameter is expected to show only mild deviations from the graphite band structure. Even small-diameter CNT show on average similarities in overall DOS shape to that for graphite, comparable to that presented here; see figure 1 of [36]. This is, however, the first reported detailed illustration of such good agreement.

The data for HOPG correspond to a weakly angle-resolved spectrum in normal emission [29], i.e., the Γ point is measured and therefore a large peak at 20 eV due to direct transitions from the bottom of the deepest σ band is observed. For MWNT, in contrast, due to the variety of tube orientations and the tube surface curvature, the spectra are basically an integration over a large range of take-off angles, thus tending to reflect the total DOS. The correlation with the graphite band structure is most strongly reinforced by the comparison of
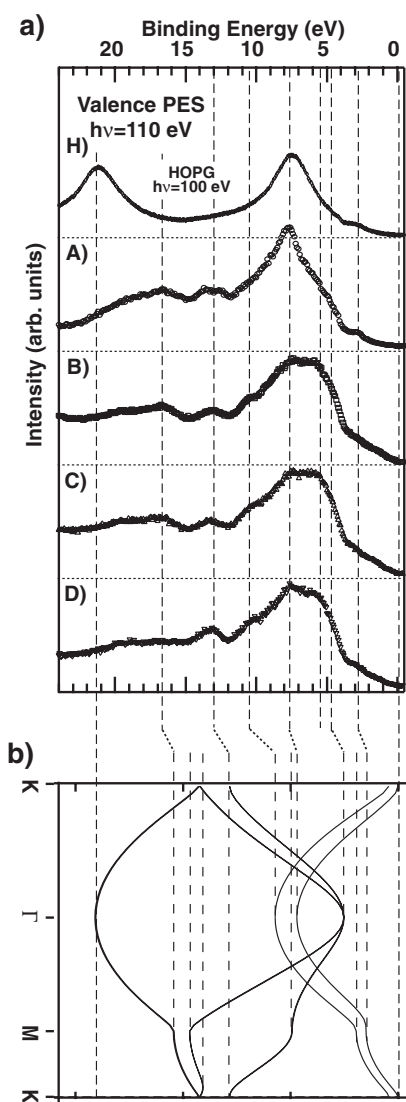
Figure 3. (a) Valence PES spectra taken at the sample positions indicated as described in figure 2. (b) The band structure (E_i versus $k_\parallel$), calculated in the full potential linear muffin-tin potential approximation [53]. The binding energy scale of the calculation has been expanded to match the bottom of the experimental bands. Matching at E_F and at the lowest σ peak leads to an expansion by 13%, similar to the 11% previously reported for graphite [35].

the valence PES at position (A) to the total graphite DOS as shown in figure 4, although the basic alignment of the critical points holds for all spectra, showing that this result is quite general for the sample.

It is striking that well-resolved structures are observed at position (A), and that all spectra reflect the critical points in spite of measurable effects of defects, although this sample showed fewer than all other spectra reported for MWNT, to our knowledge. We attribute this to the generally large distribution of the valence wavefunctions, which should tend to minimize the scattering effects of local defects. A secondary message from the MWNT data in figure 3 is that
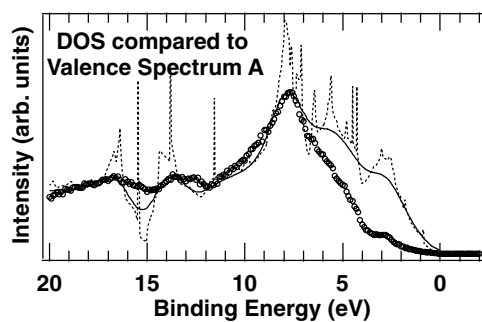
Figure 4. Valence PES spectrum compared with the total DOS of graphite from figure 2 in [53], with the energy scale expanded by a factor of 1.13 as in figure 3. The DOS was convoluted with a Gaussian (FWHM 1.4 eV) to approximately mimic the instrumental resolution and broadening due to quasiparticle lifetimes [35] and defects.

inhomogeneities such as local charging variations within a given sample do not appear to play a major role here, since the spectra line up quite well mutually (E_F and band structure critical points). The band dispersion of MWNT was the focus of a recent study [15]. Considering the rather stringent requirements necessary for proper k resolution as far as sample alignment is concerned, and the difficulties in sample preparation evidenced by the large C 1s widths reported thus far, it seems unlikely that the reported dispersion effects are due to the suggested physics.

3.4. X-ray absorption

Due both to the fact that the light spot on the sample is larger than the spot imaged by the electron detector in PES, and to the fact that the range of electron energies collected by the XAS yield detector allows multiply scattered electrons to contribute to the spectra, we do not expect a one-to-one correlation between the samples probed in XAS and PES at a given designated spot (A)–(D). Nevertheless, the overall observations are consistent between the methods, as we show in this section. Due to its local character, XAS is well suited to obtain structural information [37]. There are two aspects relevant to the present study: (1) the electronic structure is reflected in the lineshape [38]; and (2) alignment of orbitals can be probed via angle-dependent XAS [37]. The electronic structure discussion allows us to put an upper limit on the number of chemical impurities on the samples, as well as giving a separate measure of the defect density. Then, using a simple model, we investigate the expected variations in the π^* and σ^* regions of the spectra as a function of the mutual alignment of the tubes, in the appendix, and apply the result to the present data.

3.4.1. Lineshape analysis—role of defects and contaminants. As discussed in great detail elsewhere [34, 37–40], the lineshape of graphite contains two edges, one of π and one of σ symmetry. The first edge is of π symmetry, consistent with the fact that the first XAS excitation of the C 1s electron is to states just above E_F. The separation of the two symmetries corresponds well with unoccupied DOS calculations, but core hole effects are nevertheless quite important for understanding the observed lineshape [34, 38, 40, 41]. As seen in figure 5, the XAS spectra from spots (A)–(D) are similar in their overall structure to that of graphite.

There are two possible origins for deviation from the expected graphite-like lineshape: (a) non-tube structure within the sample either due to imperfections during sample synthesis or molecules adsorbed from the air during transport; and (b) defect structure within the tubes.
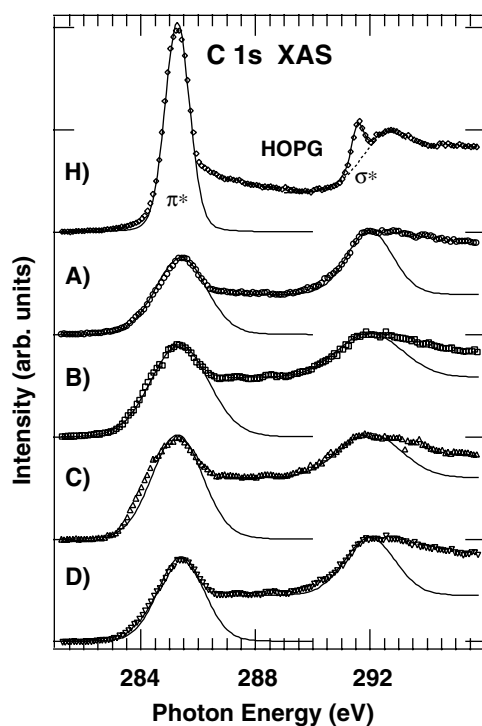
Figure 5. (A)–(D) XAS taken at the sample positions indicated. The edge resonances are fitted with Voigt functions as shown, with a Lorentzian width of 0.16 eV reflecting the estimated maximum core hole lifetime broadening. The Gaussian widths used are summarized in table 3. For the HOPG data a special background was chosen at the σ^* edge, as drawn. See the discussion in the text.

The degree of contamination (a) can be quantified via XAS, since, e.g., the π^* resonances of molecular contaminants will show distinct peaks at characteristic photon energies. No extra peaks are seen in the MWNT spectra of figure 5. Thus the maximum level of contamination can be estimated by evaluating possible peaks in the fluctuations in the experimental data[6]. From this we estimate a conservative upper limit for contamination by likely sources of 0.5%. This leaves defect structure (b) as the origin of the lineshape broadening in XAS. For contamination by graphite flakes, a different degradation of the spectrum from one approaching that of pristine graphite would be expected.

In general, defect structures (b) will cause a broadening of the XAS lineshapes, as can be seen by comparison with amorphous carbon samples. Amorphous carbon, formed by plasma deposition from methane, shows the same principal resonances in XAS as graphite [42]. Another example of graphite defect structure is provided by a sample produced by laser ablation of graphite onto a Si substrate, as reported by Gutiérrez and López [43]. Samples prepared via this method can be expected to be built of irregular arrangements of graphite flakes, and can therefore be taken as a prime example of a graphite structure with very many defects. XAS in that case shows extremely broad structures and almost no plateau between the π^* and σ^* resonances [43]. This supports the SEM analysis that our samples contain no detectable levels of such flakes. One notices that the π^* and σ^* edges are much broader for the MWNT samples

---

[6] Some likely contaminants and their strong resonance energies are the following: CO = 287.3 eV [48], CO_2 = 290 eV [49], CH_4 = 288.0 eV [50]. Fullerenes tend to have strong resonances in the region of 285 eV [51].

Table 3. Gaussian contributions to the full width at half-maximum of the Voigt functions used to fit the indicated edges of the XAS in figure 5. See the text for more details.

Position	FWHM π^* (eV)	FWHM σ^* (eV)
HOPG [40]	1.0	0.4
A	2.0	1.8
B	2.3	2.6
C	2.0	2.5
D	1.8	2.0

studied here than for HOPG, and that the fine structure of the σ^* region is not observed. We attribute these observations to defects in the ideal tube structure, as we discuss in more detail below, but comparison to the available spectra of amorphous graphite [42–44] suggests that the concentration of defects is low. Their existence in the samples would imply a partial breakdown of the distinction between π^* and σ^* portions of the DOS, which the broadening in the spectra clearly reflects. Probably minor modifications in the intensity ratios can be expected due to rehybridization, which is found theoretically for small tubes [45], or to the presence of different defects/allotropes. However, the similarity of the overall spectral distribution motivates us to consider the spectra in terms of the two symmetries, and this approach can be expected to improve with sample homogeneity.

Because XAS measures the core hole-perturbed DOS within a few atomic sites of the excited atom [38], the broadening in the π^* and σ^* edges compared to those for HOPG is consistent with chemical shifts expected to be associated with local defect structures [42, 44]. To quantify the spectral consequences of disorder in XAS in a simple manner, we simulate the resonances with Voigt functions, as illustrated and described in figure 5. We compare the Gaussian broadening contributions from these simulations in table 3. The variation in width at the π^* and σ^* resonances, which change (approximately) in parallel, show the same trend as the C 1s and valence PES data, in that spectra acquired at spot (A) have a small width. The spectra from positions B and C are notably broader than those from positions (A) and (D).

We reiterate that in graphite, wavefunctions corresponding to the π^* and σ^* peaks have a spatial extent of a few bond lengths [38], similar to those for the lowest π^* band of C_{60} [46]. In both cases, the emphasis is on sites at and immediately adjacent to the core-excited atom. This suggests that similar local sensitivities are to be expected for all CNT varieties, from SWNT to MWNT. Thus we assume that the broad structure in XAS is due to defects on a scale of a few bond lengths, i.e., a local distortion in the structure, which would be consistent with the local sensitivity in C 1s and apparent lack thereof in valence PES data. This local sensitivity also rationalizes the lack of diameter dependence seen in the π^* region found in an EELS study of single-walled and multiwalled CNT [11].

3.4.2. Spectral intensity—measuring CNT orientation. In the following we want to focus on the spectral intensity in XAS. Oriented nanotubes are expected to show variations in the relative intensities of the σ^* and π^* portions of the spectra as a function of light incidence angle. The spectra (A) and (D) in figure 5 were taken at normal incidence, spectrum (B) at 70° from the normal, and spectrum (C) at 80° from the sample normal. Spectrum (A) was taken with a retardation voltage of 210 V, whereas all other spectra were taken in total electron yield mode. We now take up in more detail the two aspects of the data introduced immediately above.

Focusing only on the geometric aspects, one can imagine some extreme cases, such as excitation with the polarization vector along the axis of a CNT, for which only σ^* states are
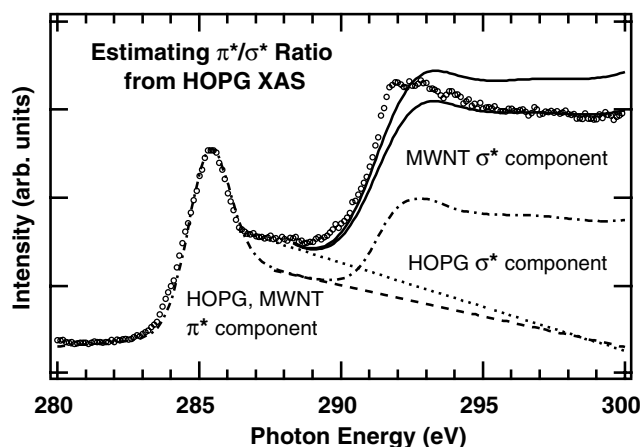
Figure 6. Illustration of the method used to obtain the ratio of the σ^* and π^* components in XAS for spot (A) (circles), making use of the broadened HOPG spectrum [40] (dashed–dotted curve) taken at a light incidence angle of 45°. The original HOPG spectrum is shown in figure 5. The assumed π^* backgrounds for the HOPG (dashed curve) and MWNT (dotted curve) data are indicated. To isolate the σ^* component of the HOPG data, the assumed π^* background is subtracted from the broadened spectrum. The resulting isolated HOPG σ^* component is added to the assumed MWNT π^*-derived background and scaled by factors of 1.8 and 2.2 (solid curves) to estimate the limits of the actual scale factor in the σ^* region, giving a geometrical ratio π^*/σ^* of 0.50 ± 0.06. Because we focus on the σ^* threshold region, this ratio is only mildly sensitive to the choice of background, and the error should lie within the given margins.

accessible, in analogy with excitation of graphite with the polarization in the plane of the layers. Polarization perpendicular to a CNT axis will excite σ^* and π^* states equally, albeit from different portions of a given CNT. We show in the appendix how these contributions are calculated. Note that the range of possible values of this ratio for oriented CNT is between 0 and 1, and that an angle-independent π^*/σ^* intensity ratio of 0.33 is expected for isotropically distributed CNT orientations. Below we will apply this to gain information about the average near-surface orientations in our sample. However, first it is necessary to develop a means of estimating the ratio from C 1s XAS spectra. To accomplish this, we take HOPG as the standard, and examine XAS at a 45° incidence angle, for which the geometrical factor is then identically 1 [37]. To obtain the ratio of π^*/σ^* in the present work the HOPG spectrum is broadened and scaled to match the π^* resonance, as illustrated in figure 6.

As summarized in table 4, for grazing light incidence the π^* intensity increases, which suggests, as can be inferred from the derivations in the appendix, that tubes at the surface of our samples tend to lie parallel to the substrate. Because the spectra are averaged over many hundreds of micrometres along the surface, it is not possible to consider the alignment at a greater level of detail, but the method lends itself to rapid assessment of the average tube alignment.

4. Conclusions

Valence and core level spectra of the present MWNT sample show a variation in shape depending on the sample position. Defect densities near the surface of the sample are found to vary considerably, with some spots showing almost no sign of defects/contamination, and representing the present state-of-the-art. The width and background of the C 1s line vary in concert as a function of sample position, and a similar correlation is observed for the

Table 4. Geometry-derived ratios of π^*/σ^* as estimated by the procedure described in the text and illustrated in figure 6 for the positions indicated. The ratio for an isotropic distribution is calculated in the appendix.

Position	Incidence angle (deg)	π^*/σ^*
A	0	0.50 ± 0.06
B	70	0.90 ± 0.06
C	80	1.00 ± 0.06
D	0	0.60 ± 0.06
Isotropic distribution		0.33

backgrounds in valence and C 1s PES. In all cases we can identify graphite band structure-derived signals in valence PES, notably the DOS maxima. From the assignment of the valence peaks we interpret the spectra as representing an integration over the graphite Brillouin zone. Effects of this nature are to be expected in a simple model, since the MWNT are cylindrical, presenting different effective emission angles from a given CNT, and are not generally well ordered at the surface of the sample, both effects causing a sampling of virtually all possible local surface orientations. XAS follows the strong variation as a function of sample position found in valence and C 1s PES. XAS data are quite similar to the absorption of pure graphite, reflecting simple broadening effects due to disorder in the nanotube walls. The local sensitivity of XAS rationalizes the lack of diameter dependence of the π^* portion of the spectra for CNT of widely differing diameters [11].

It is important to note that the measurement techniques used here are not sensitive to small changes in the DOS near E_F. Techniques such as transport measurements could therefore obtain qualitatively different results on the same samples. For structurally uniform samples which would be more likely to consistently display small intrinsic deviations from the simple picture of graphite, high resolution PES would also show such deviations.

Appendix. Nanotube orientation determined with C 1s XAS

Here we present a simple estimate of the π^* and σ^* intensities for an isotropic distribution of tube orientations. The fundamental assumption of our analysis is that the spectrum can be divided into invariable π^* and σ^* contributions, whose relative weights vary depending on the geometrical factors. Simple considerations show that aligned CNT are expected to have a strong angle dependence in XAS as a function of light incidence angle and tube orientation in the ratio of π^* to σ^* intensities. The expected angular distribution for three principal nanotube–sample–x-ray orientations are shown in figure A.1. To investigate this in detail, we make the assumption that a local surface section can be approximated as an equivalent area of graphene. This allows us to make use of the simple angle dependence expected for graphene [37] via elementary geometrical considerations.

To calculate XAS intensities the angle between the tube axis and the polarization vector **E** is important. For the calculation we use two frames of reference. The first is the laboratory

Variation in the 1s XAS cross section of the π* and σ* orbitals with x-ray incidence angle on cylindrical graphene
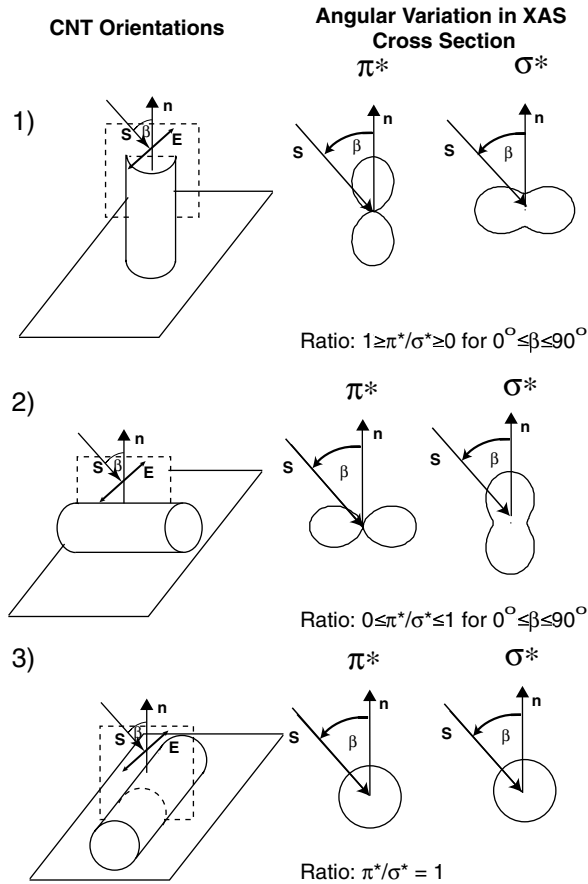

Figure A.1. Left: an illustration of three fundamental CNT orientations for the determination of sample alignment using XAS; and right: the corresponding angular dependences of the π^* and σ^* intensities expected from the geometrical factors. The Poynting vector **S** and polarization vector **E** are in all cases in the plane of the page (also given by the dashed rectangle), whereas the cylinder which symbolizes a CNT is perpendicular to (case 1) or lies in the substrate surface plane (cases 2 and 3). The vector **n** is the normal to the substrate surface (solid rectangle), and β denotes the x-ray incidence angle with respect to the sample normal **n**. The geometrical π^*/σ^* ratio varies between 0 and 1 for different orientations.

frame, denoted by **x**, **y**, and **z**, with the polarization **E** along the z-axis. The CNT reference frame is denoted by **x′**, **y′**, and **z′**, with the tube axis oriented along the z'-axis. Figure A.2 illustrates a cross section of a tube, with the π^* orbitals oriented radially in the $x'y'$-plane, and the σ^* orbitals oriented tangent to the solid circle shown, as well as parallel to the z'-axis. We begin with the π^* contribution.

For this we express the circle normal **n′** as a function of both angles shown in figure A.2 (see, e.g., [47]),

$$\mathbf{n}'_{\phi,\alpha} = (\cos\phi, \cos\alpha\sin\phi, \sin\alpha\sin\phi). \tag{A.1}$$

**Illustration of the coordinates
used for the intensity calculation**

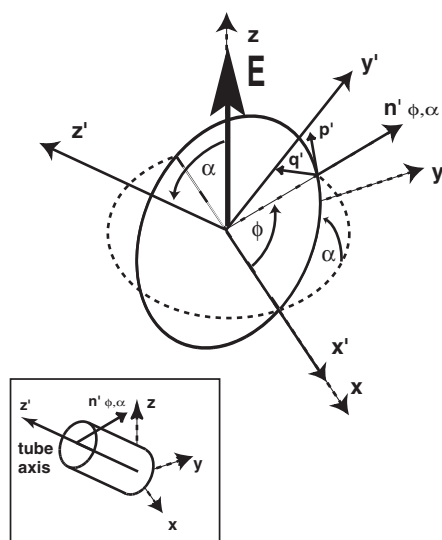**Figure A.2.** An illustration of the two frames of reference used in the calculation: the laboratory frame $(\mathbf{x}, \mathbf{y}, \mathbf{z})$ and the CNT frame $(\mathbf{x}', \mathbf{y}', \mathbf{z}')$. The vector $\mathbf{E}$ is along the z-axis, whereas the CNT axis is along the z'-axis, as shown in the inset. The angle α describes the rotation around the x-axis; the angle ϕ describes the rotation around the z'-axis. The disc in the coordinate system corresponds to one slice of the CNT, dashed in the laboratory frame of reference, solid after rotation through the angle α. The π^* orbitals are parallel to the local normal of the CNT $\mathbf{n}'$. The plane of the σ^* orbitals is determined by the vectors $\mathbf{p}'$ and $\mathbf{q}'$.

The local contribution to the π^* XAS intensity is proportional to the square of the scalar product of this local normal and $\mathbf{E}$, which can be taken to have unit length. This product is

$$[\mathbf{n}'_{\phi,\alpha} \cdot (0, 0, 1)]^2 = \sin^2 \alpha \sin^2 \phi. \tag{A.2}$$

Hence the differential intensity is

$$\mathrm{d}I_{\pi^*}^{\mathrm{CNT}} = I_{\pi^*}^0 \sin^2 \alpha \sin^2 \phi \, \mathrm{d}\phi \, \mathrm{d}\alpha, \tag{A.3}$$

where $I_{\pi^*}^0$ is the squared C 1s $\rightarrow \pi^*$ matrix element, to which we return below. Integration over all unique values of α, and also accounting for the entire tube circumference by integrating over ϕ, gives the total intensity to within a constant factor:

$$I_{\pi^*}^{\mathrm{CNT}} = I_{\pi^*}^0 \frac{\pi^2}{4}.$$

Now we consider the σ^* contribution. The local azimuthal orientation is unimportant, since it is only required to calculate the projection of $\mathbf{E}$ on the local surface tangent plane. This plane can be defined by taking two vectors which are perpendicular to $\mathbf{n}_{\phi,\alpha}$. One vector which conveniently satisfies this requirement is the tangent to the circle, which is equivalent to the surface normal at $\phi + \frac{\pi}{2}$:

$$\mathbf{p}'_{\phi,\alpha} = \mathbf{n}'_{\phi + \frac{\pi}{2}, \alpha}$$
$$= \left(\cos\left(\phi + \frac{\pi}{2}\right), \cos\alpha \sin\left(\phi + \frac{\pi}{2}\right), \sin(\alpha) \sin\left(\phi + \frac{\pi}{2}\right) \right)$$
$$= (-\sin\phi, \cos\alpha \cos\phi, \sin\alpha \cos\phi).$$

A second such vector $\mathbf{q}'_{\phi,\alpha}$, which is perpendicular to both of the above, is the cross product

$$
\begin{aligned}
\mathbf{q}'_{\phi,\alpha} &= \mathbf{n}'_{\phi,\alpha} \times \mathbf{p}'_{\phi,\alpha} \\
&= (x, y, \cos\alpha \cos^2\phi + \cos\alpha \sin^2\phi) \\
&= (x, y, \cos\alpha).
\end{aligned}
$$

The x and y terms in $\mathbf{q}'_{\phi,\alpha}$ can be ignored, since they are not needed in what follows. These vectors are illustrated in figure A.2. The direction cosines of $\mathbf{E}$ relative to these two vectors [47] form the components of the projection sought; these, when squared, yield the σ^* intensity factor needed. In analogy to the case for the π^* intensity, the differential intensity is therefore

$$
\begin{aligned}
\mathrm{d}I_{\sigma^*} &= I^0_{\sigma^*}[(\mathbf{p}'_{\phi,\alpha} \cdot (0, 0, 1))^2 + (\mathbf{q}'_{\phi,\alpha} \cdot (0, 0, 1))^2]\,\mathrm{d}\phi\,\mathrm{d}\alpha \\
&= I^0_{\sigma^*}[\cos^2\alpha + \sin^2\alpha \cos^2\phi]\,\mathrm{d}\phi\,\mathrm{d}\alpha.
\end{aligned}
$$

Integrating to get the total intensity for all angles gives

$$
I^{\mathrm{CNT}}_{\sigma^*} = I^0_{\sigma^*}\frac{3\pi^2}{4}.
$$

This simple calculation shows that the π^* portion of the spectrum is de-emphasized by a factor of three relative to the σ^* for the isotropically distributed ensemble, or

$$
\left(\frac{I^{\mathrm{CNT}}_{\pi^*}}{I^{\mathrm{CNT}}_{\sigma^*}}\right)_{\mathrm{isotropic}} = \frac{I^0_{\pi^*}}{3I^0_{\sigma^*}}.
$$

The factors $I^0_{\pi^*}$ and $I^0_{\sigma^*}$ are needed to complete the estimate. Examining graphite XAS data at $45°$ incidence, which should excite π^* and σ^* with equal geometric factors, we can identify the σ^* and π^* cross sections for graphite as being proportional to the intrinsic ones, giving

$$
\left(\frac{I^{\mathrm{G}}_{\pi^*}}{I^{\mathrm{G}}_{\sigma^*}}\right)_{45°} = \frac{I^0_{\pi^*}}{I^0_{\sigma^*}}.
$$

In practice, we have chosen to use these HOPG data as a template, and to manipulate them to obtain the geometrical intensity factors in the MWNT data, as illustrated in figure 6.

It is worth pointing out that the results for CNT within these approximations are the same for all varieties of straight cylindrical tube. The same result could have been obtained with the concept that the E-field polarized along the axis yields only σ^* contributions, and polarized perpendicular to the axis yields equal geometric factors for σ^* and π^*. The total spectrum of a given ensemble of tubes and for a given incident light polarization, if the tube orientations are known, can then be estimated as a linear combination of these two extreme geometries. Thus, a uniform distribution contains equal amounts of the two geometries, giving a geometric intensity factor of

$$
0.5(I_{\sigma^*} + (0.5I_{\sigma^*} + 0.5I_{\pi^*})) = 0.75I_{\sigma^*} + 0.25I_{\pi^*}
$$

as expected. The advantage of the derivation above is that it can be used as the basis for more complex geometrical distributions, as well. It also simplifies consideration of the spectra in general, e.g., suggests that it is impossible for both π^* and σ^* contributions in XAS to increase or decrease in parallel [19] for samples consisting of cylindrical tubes.

References

[1]   Maarouf A A, Kane C L and Mele E J 2000 *Phys. Rev.* B **61** 11156
[2]   Lambin P, Meunier V and Rubio A 2000 *Phys. Rev.* B **62** 5129
[3]   Dresselhaus M S, Dresselhaus G and Saito R 1992 *Phys. Rev.* B **45** 6234
[4]   Knupfer M 2001 *Surf. Sci. Rep.* **42** 1
[5]   Saito R, Dresselhaus G and Dresselhaus M S 1993 *J. Appl. Phys.* **73** 494
[6]   Wildöer J W G, Venema L C, Rinzler A G, Smalley R E and Dekker C 1998 *Nature* **391** 59
[7]   Eisebitt S, Karl A, Eberhardt W, Fischer J E, Sathe C, Agui A and Nordgren J 1998 *Appl. Phys.* A **67** 89
[8]   Haggenmueller R, Gommans H H, Rinzler A G, Fischer J E and Winey K I 2000 *Chem. Phys. Lett.* **330** 219
[9]   Rohmund F, Falk L K L and Campbell E E B 2000 *Chem. Phys. Lett.* **328** 369
[10] Cao A, Xu C, Liang J, Wu D and Wei B 2001 *Chem. Phys. Lett.* **344** 13
[11] Stéphan O, Kociak M, Henrard L, Suenaga K, Gloter A, Tencé M, Sandré E and Colliex C 2001 *J. Electron Spectrosc. Relat. Phenom.* **114** 209
[12] Liu X, Pichler T, Knupfer M, Golden M S, Fink J, Walters D A, Casavant M J, Schmidt J and Smalley R E 2001 *Synth. Met.* **121** 1183
[13] Zhang W D, Wen Y, Liu S M, Tjiu W C, Xu G Q and Gan L M 2002 *Carbon* **40** 1985
[14] Chen P, Wu X, Lin J, Ji W and Tan K L 1999 *Phys. Rev. Lett.* **82** 2548
[15] Choi J, Lee S M, Choi Y C, Lee Y H and Jiang J C 2001 *Chem. Phys. Lett.* **349** 185
[16] Suzuki S, Bower C, Kiyokura T, Nath K G, Watanabe Y, Zhu W and Zhou O 2001 *J. Electron Spectrosc. Relat. Phenom.* **114** 225
[17] Goldoni A, Larciprete R, Gregoratti L, Kaulich B, Kiskinova M, Zhang Y, Dai H, Sangaletti L and Parmigiani F 2002 *Appl. Phys. Lett.* **80** 2165
[18] Ago H, Kulger T, Cacianlli F, Salaneck W R, Shaffer M S P, Windle A H and Friend R H 1999 *J. Phys. Chem.* B **103** 8116
[19] Chiou J W *et al* 2002 *Appl. Phys. Lett.* **81** 4189
[20] Suzuki S, Kiyokura T, Nath K G, Ogino T, Heun S, Zhu W, Bower C and Zhou O 2001 *Phys. Rev.* B **63** 245418
[21] Brühwiler P A 2001 *J. Phys.: Condens. Matter* **13** 11229
[22] Nyholm R, Svensson S, Nordgren J and Flodström A 1986 *Nucl. Instrum. Methods* A **246** 267
[23] Andersen J N, Björneholm O, Sandell A, Nyholm R, Forsell J, Thånell L, Nilsson A and Mårtensson N 1991 *Synchrotron Radiat. News* **4** (4) 15
[24] Charlier J C and Michenaud J P 1993 *Phys. Rev. Lett.* **70** 1858
[25] Ebbessen T W and Ajayan P M 1992 *Nature* **358** 220
[26] Drotar J T, Wei B Q, Zhao Y-P, Rammanath G, Ajayan P M, Lu T-M and Wang G-C 2001 *Phys. Rev.* B **64** 125417 and references therein
[27] Schnadt J, Schiessling J, O'Shea J N, Patthey L, Shi M, Puglia C, Mårtensson N and Brühwiler P A 2001 *Nucl. Instrum. Methods* B **184** 609
[28] Hüfner S 1996 *Photoelectron Spectroscopy* (Berlin: Springer)
[29] Bennich P, Puglia C, Brühwiler P A, Nilsson A, Maxwell A J, Sandell A, Mårtensson N and Rudolf P 1999 *Phys. Rev.* B **59** 8292
[30] Prince K C, Ulrych I, Peloi M, Ressel B, Chab V, Crotti C and Comicioli C 2000 *Phys. Rev.* B **62** 6866
[31] Balasubramanian T, Andersen J N and Walldén L 2001 *Phys. Rev.* B **64** 205420
[32] Rotenberg E, Enkvist C, Brühwiler P A, Maxwell A J and Mårtensson N 1996 *Phys. Rev.* B **54** R5279
[33] Osborne S J, Ausmees A, Svensson S, Kivimäki A, Sairanen O-P, Naves de Brito A, Aksela H and Aksela S 1995 *J. Chem. Phys.* **102** 7317
[34] Brühwiler P A, Karis O and Mårtensson N 2002 *Rev. Mod. Phys.* **74** 703
[35] Heske C, Treusch R, Himpsel F J, Kakar S, Terminello L J, Weyer H J and Shirley E L 1999 *Phys. Rev.* B **59** 4680
[36] Larciprete R, Lizzit S, Botti S, Cepek C and Goldoni A 2002 *Phys. Rev.* B **66** 121402(R)
[37] Stöhr J 1992 *NEXAFS Spectroscopy* (Berlin: Springer)
[38] Ahuja R, Brühwiler P A, Wills J M, Johansson B, Mårtensson N and Eriksson O 1996 *Phys. Rev.* B **54** 14396
[39] Batson P E 1993 *Phys. Rev.* B **48** 2608
[40] Brühwiler P A, Maxwell A J, Puglia C, Nilsson A, Andersson S and Mårtensson N 1995 *Phys. Rev. Lett.* **74** 614
[41] Ma Y, Skytt P, Wassdahl N, Glans P, Mancini D C, Guo J and Nordgren J 1993 *Phys. Rev. Lett.* **71** 3725
[42] Comelli G, Stöhr J, Robinson C J and Jark W 1988 *Phys. Rev.* B **38** 7511
[43] Gutiérrez A and López M F 1995 *Europhys. Lett.* **31** 299
[44] Diaz J, Anders S, Zhou X, Moler E J, Kellar S A and Hussain Z 1999 *J. Electron Spectrosc. Relat. Phenom.* **101** 545

[45] Kleiner A and Eggert S 2001 *Phys. Rev.* B **64** 113402
[46] Maxwell A J, Brühwiler P A, Arvantis D, Hasselström J and Mårtensson N 1997 *Phys. Rev. Lett.* **79** 1567
[47] Goldstein H 1981 *Classical Mechanics* (Reading, MA: Addison-Wesley)
[48] Hitchcock A P and Brion C E 1980 *J. Electron Spectrosc. Relat. Phenom.* **18** 1
[49] Wight G R and Brion C E 1974 *J. Electron Spectrosc. Relat. Phenom.* **3** 192
[50] Kosugi N 1996 *J. Electron Spectrosc. Relat. Phenom.* **79** 351
[51] Rudolf P, Golden M S and Brühwiler P A 1999 *J. Electron Spectrosc. Relat. Phenom.* **100** 409
[52] Umishita K, Ochiai Y, Iwasaki K and Hino S 2001 *Synth. Met.* **121** 1159
[53] Ahuja R, Auluck S, Trygg J, Wills J M, Eriksson O and Johansson B 1995 *Phys. Rev.* B **51** 4813